APSB

ORIGINAL ARTICLE

Transferrin receptor-targeted immunostimulant for photodynamic immunotherapy against metastatic tumors through β-catenin/CREB interruption

Mengyi Yan [a], **Xiayun Chen** [a], **Xiaotong Li** [b], **Qianqian Liu** [a], **Baixue Yu** [a], **Yi Cen** [a], **Wei Zhang** [a], **Yibin Liu** [a], **Xinxuan Li** [a], **Ying Chen** [a], **Tao Wang** [c,*], **Shiying Li** [a,d,*]

[a]*The Fifth Affiliated Hospital, Guangdong Provincial Key Laboratory of Molecular Target & Clinical Pharmacology, the NMPA and State Key Laboratory of Respiratory Disease, the School of Pharmaceutical Sciences, Guangzhou Medical University, Guangzhou 511436, China*
[b]*Department of Anesthesiology, the Second Clinical School of Guangzhou Medical University, Guangzhou 511436, China*
[c]*State Key Laboratory of Respiratory Diseases, Guangdong Key Laboratory of Vascular Diseases, Guangzhou Institute of Respiratory Health, the first Affiliated Hospital, Guangzhou Medical University, Guangzhou 510120, China*
[d]*Department of Pulmonary and Critical Care Medicine, Zhujiang Hospital, Southern Medical University, Guangzhou 510280, China*

Abstract The immunosuppressive phenotype of tumor cells extensively attenuates the immune activation effects of traditional treatments. In this work, a transferrin receptor (TfR) targeted immunostimulant (PTI) is fabricated for photodynamic immunotherapy against metastatic tumors by interrupting β-catenin signal pathway. To synthesize PTI, the photosensitizer conjugated TfR targeting peptide moiety (Palmitic-K(PpIX)-HAIYPRH) is unitized to encapsulate the transcription interrupter of ICG-001. On the one hand, the recognition of PTI and TfR can promote drug delivery into tumor cells to destruct primary tumors through photodynamic therapy and initiate an immunogenic cell death with the release of tumor-associated antigens. On the other hand, PTI will interrupt the binding between β-catenin and cAMP response element-binding protein (CREB), regulating the gene transcription to downregulate programmed death

*Corresponding authors.

E-mail addresses: taowang@gzhmu.edu.cn (Tao Wang), lisy-sci@gzhmu.edu.cn (Shiying Li).

C−C motif chemokine ligand 4	ligand 1 (PD-L1) while upregulating C−C motif chemokine ligand 4 (CCL4). Furthermore, the elevated CCL4 can recruit the dendritic cells to present tumor-specific antigens and promote T cells activation and infiltration, and the downregulated PD-L1 can avoid the immune evasion of tumor cells and activate systemic anti-tumor immunity to eradicate lung metastasis. This work may inspire the development of antibody antibody-free strategy to activate systemic immune response in consideration of immunosuppressive conditions.

1. Introduction

Tumor cells evade the immune clearance by altering their immunosuppressive phenotype[1], which will also attenuate the immunological function of T cells through the paracrine pathway[2-6]. Among which, the elevated expression of the immune checkpoint can directly reduce the recognition and activation of cytotoxic T cells, resulting in malignant tumor growth and poor immunotherapeutic prognosis[7]. Especially, programmed death ligand 1 (PD-L1) as one of the major immunosuppression checkpoints is overexpressed in most malignancies to diminish effector T cells response and escape immune attack[8,9]. To solve it, traditional immune checkpoint blockade (ICB) by using anti-PD-L1 can restore the immune activity of T cells[10]. Even so, a low response rate is received in the current ICB due to the restricted tumor penetration of antibodies and the immunosuppressive tumor microenvironment. Alternatively, the expression of PD-L1 can be also regulated at a transcription level[11-13], which may provide an antibody-free strategy to reactivate the systemic anti-tumor immunity. Of note, the aberrant activation of the β-catenin signal pathway is closely associated with the malignant tumor progression[14], invasion[15], metastasis[16], and recurrence[17], which is also attributed to the T cells exclusion and immune resistance[18]. However, the underlying mechanism is waiting to be discovered, and the immune activation effect is rarely investigated through a chemotherapeutic interruption strategy.

Apart from regulating gene transcription, recent studies confirmed that chemotherapeutic drugs could also initiate immunogenic cell death (ICD) of tumor cells to release tumor-associated antigens (TAAs)[19,20]. Such an ICD effect can provide tumor-specific and whole antigens to initiate anti-tumor immunity, showing great advantages over artificially synthesized antigens. Among which, photodynamic therapy (PDT) is a historically and clinically available modality for superficial tumor treatment, possessing unique characteristics such as a light-controlled manner, no drug resistance and good biosafety[21]. Mechanistically, an appropriate light irradiation can activate the photosensitizer to an excited state, which subsequently transfers the energy to the nearby oxygen (O_2) to produce reactive oxygen species (ROS) causing oxidative damage to biological components for cell destruction[22]. Moreover, the robust PDT is always accompanied with the release of TAAs, such as adenosine triphosphate (ATP) release, calreticulin (CRT) exposure and high mobility group protein 1 (HMGB1) translocation. However, PDT alone still cannot activate an effective immunotherapy despite potentiating the ICD effect, resulting from the immunosuppressive phenotype of tumor cells. Therefore, chemotherapy reprogramming the immunosuppressive tumor phenotype may provide a perspective strategy to activate systemic anti-tumor immunity in combination with PDT.

To amplify the synergistic effect and avoid unwanted side effects, drug combinations should be delivered to the tumor site to reduce systemic drug exposure and exert their pharmacological activities. Especially, the recognition of tumor-specific receptors and targeting ligands can facilitate the drug targeting delivery. Transferrin receptor (TfR) is an essential transmembrane glycoprotein overexpressed in rapidly proliferating tumor cells due to the high demands of iron[23]. In consideration of the above scenarios, a TfR-targeted immunostimulant (PTI) was designed for photodynamic immunotherapy by interrupting the β-catenin signal pathway. For the preparation of PTI, the photosensitizer of protoporphyrin IX (PpIX) and hydrophobic palmitic acid were conjugated onto the TfR-targeting peptide sequence (HAIYPRH)[24] to encapsulate the transcription interrupter of ICG-001 (Scheme 1A). Nanosized PTI was preferable to accumulate at the 4T1 solid tumor with TfR overexpression and the initiated PDT would destruct the primary tumor while inducing an ICD effect to release TAAs (Scheme 1B). Besides, PTI utilized ICG-001 to interrupt the binding between β-catenin and cAMP response element-binding protein (CREB), regulating the gene transcription to downregulate PD-L1 and upregulate C−C motif chemokine ligand 4 (CCL4). Advantageously, the PD-L1 reduction could facilitate the immune recognition and clearance of tumor cells for enhanced systemic anti-tumor immunity. Moreover, the increased CCL4 level would promote the recruitment of dendritic cells (DCs) to present tumor-specific antigens and enhance T cells activation and infiltration for lung metastatic suppression[25]. Such a rationally designed immunostimulant provided an antibody-free strategy to activate systemic anti-tumor immunity, which might facilitate the development of immunotherapy by using traditional treatments.

2. Materials and methods

2.1. Materials

ICG-001 was purchased from MCE Medchemexpress Co., Ltd. (Shanghai, China). N,N'-Dimethylformamide (DMF), dimethyl sulfoxide (DMSO), dichloromethane and methanol were acquired from Shanghai Titan Scientific Co., Ltd. (Shanghai, China). PpIX was provided by Shanghai Yuanye Biotechnology Co., Ltd. (Shanghai, China). O-Benzotriazol-1-yl-tetramethyluronium hexafluorophosphate (HBTU) was obtained from Shanghai Aladdin Biochemical Technology Co., Ltd. (Shanghai, China). N-Hydroxybenzotrizole (HOBt) was purchased from Shanghai Macklin Biochemical Co., Ltd. (Shanghai, China). All the fluorenemethoxycarbonyl (Fmoc) protected amino acids were acquired from GL Biochem Ltd. (Shanghai, China), including Fmoc-His(Trt)-OH, Fmoc-Ala-OH, Fmoc-Ile-OH,
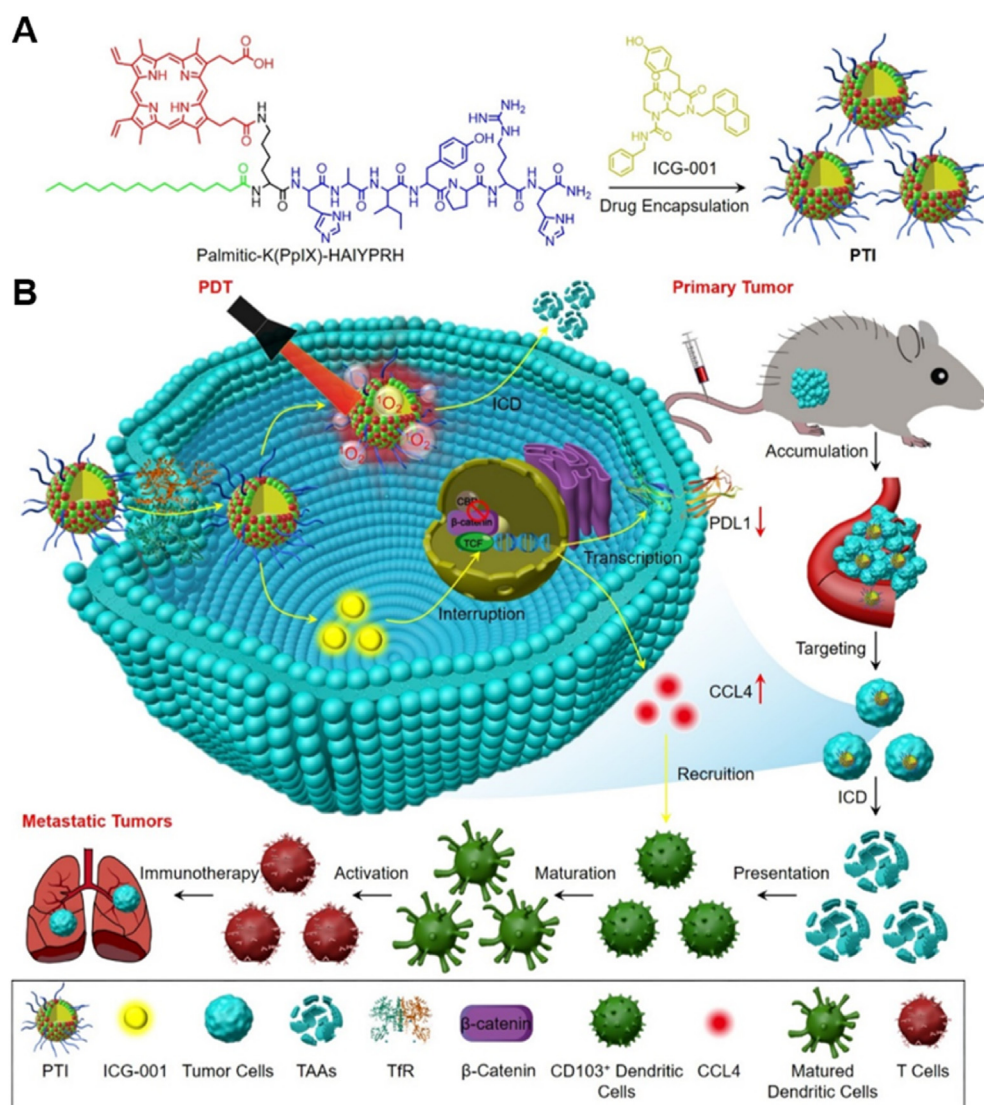
Scheme 1 Chemical structure and the proposed mechanism of PTI to eradicate metastatic tumors through photodynamic immunotherapy. (A) Chimeric peptide of (Palmitic-K(PpIX)-HAIYPRH) can load ICG-001 to self-assemble into nanomedicine for preparation of PTI; (B) PTI is preferred to accumulate in primary tumor site through TfR mediated tumor targeting drug delivery. In tumor cells, PTI can not only interrupt the β-catenin/CREB recognition and regulate gene transcription to decrease PD-L1 expression and elevate CCL4 expression, but also trigger the release of tumor associated antigens (TAAs) through photodynamic therapy (PDT) induced immunogenic cell death (ICD). The released CCL4 can recruit dendritic cells (DCs), combining with TAAs to accelerate the DCs maturation, T cells activation and infiltration for metastatic tumor eradication.

Fmoc-Tyr(*t*Bu)-OH, Fmoc-Pro-OH, Fmoc-Arg(pbf)-OH and Fmoc-Lys(Mtt)-OH. Dulbecco's modified Eagle's medium (DMEM, VivaCell) and fetal bovine serum (FBS, VivaCell) were got from Shanghai XP Biomed Ltd. (Shanghai, China). The pen strep (PS, Gibco) was bought from ThermoFisher Biochemical Products (Beijing) Co., Ltd. (Beijing, China). Reactive oxygen species assay kit, MTT cell proliferation and cytotoxicity assay kit, Hoechst 33342 and Annexin V-FITC apoptosis detection kit were purchased from Beyotime Biotechnology (Shanghai, China). Singlet oxygen sensor green (SOSG) was bought from Meilunbio (Dalian, China). Calcein-AM/PI double stain kit came from Yeasen Biotechnology Co., Ltd. (Shanghai, China).

2.2. Cell culture

Mouse breast cancer cells (4T1), human non-small cell lung cancer cells (A549) and human embryonic kidney cells (293T) were cultured at DMEM supplemented with 10% FBS and 1% PS in a 37 °C incubator with 5% CO_2.

2.3. Synthesis of PTI

PT (Palmitic-K(PpIX)-HAIYPRH) was constructed by conjugating the TfR targeting peptide with photosensitizer using solid-phase synthesis. After extraction and purification by glacial ether, the peptide was dried in a vacuum oven overnight. The solutions

of PT (100 g/L in DMSO) and ICG-001 (50 g/L in DMSO) were mixed at the mass ratio of 10:4 and subsequently added to distilled water under ultrasound. The dialysis system (MWCO = 1000 D) was used to separate drug-loaded nanoparticles. The targeted nano immunostimulant coupled with photosensitizer was obtained through separation and named PTI.

2.4. Characterization of PTI

The morphological characterization was observed by transmission electron microscopy (TEM, ZEISS, ELYPA P.1, Shanghai, China). The particle size and zeta potential of PTI were determined by a diameter analyzer (Malvern Panalytical Ltd., ZETASIZER NANO ZS, US). The drug loading of ICG-001 in PTI was quantified by high performance liquid chromatography (HPLC, Shimadzu global laboratory consumables Co., Ltd., LC-20AT, Shanghai, China). UV−Vis spectrophotometer (Shimadzu global laboratory consumables Co., Ltd., UV-2600, Shanghai, China) was utilized to quantify PpIX and measure the UV−Vis spectra of PpIX, ICG-001, PT and PTI in DMSO. The photo-thermal performance of PTI was evaluated using a thermal imager (FLUKE INTERNATIONAL CORPORATION, Fluke Ti480 PRO, Shanghai, China). PTI and PT were photographed by thermal imagers to detect temperature changes before and after 15-min irradiation (638 nm).

The drug release behavior of ICG-001 was studied at pH 6.5. In brief, 2 mL of PTI was put in a dialysis bag (MWCO = 1000 D) and placed in a tube containing 15 mL of acidic buffer (pH = 6.5). Incubate it in a shaking table at 37 °C, and collect liquid from the tube at regular intervals for HPLC analysis. The same volume of liquid as the extracted amount must be replenished into the tube to ensure that the volume of liquid in the tube remained unchanged.

SOSG, which is sensitive to $^1O_2$, can be employed for $^1O_2$ detection. PT (4.73 mg/L), ICG-001 (1.12 mg/L), PT (4.73 mg/L) + ICG-001 (1.12 mg/L), and PTI (5.85 mg/L) were incubated individually with SOSG (2.5 μmol/L) and then illuminated under 638 nm light with various periods of time (10 s). The generated $^1O_2$ was determined by the recovered SOSG fluorescence under 521 nm excitation.

2.5. Cell internalization

Confocal laser scanning microscope (CLSM, Carl Zeiss (Shanghai) Co., Ltd., ELYPA P.1, Shanghai, China) and flow cytometry analysis were exploited to observe the cell internalization of PT and PTI by 4T1 cells. For CLSM imaging, 4T1 cells were cultured for 6 h with different concentrations of PTI (23.4, 46.8, 93.6 mg/L) or PT (18.7, 37.4, 74.9 mg/L). On the other hand, 4T1 cells were cultured with PTI (46.8 mg/L) or PT (37.4 mg/L) in the dark for different incubation time (3, 6 and 9 h). After washing with PBS for three times, the cells were labeled with Hoechst 33342 and imaged by CLSM. The same groups were set for flow cytometry analysis (Beckman Coulter Commercial Enterprise Co., Ltd., CytoFLEX S.4, Shanghai, China). But the incubated cells were digested and washed with PBS. The fluorescence intensity of cells was detected by flow cytometry.

2.6. Production of ROS in cells

4T1 cells were incubated with ICG-001 (11.2 mg/L), PT (47.3 mg/L), PT (47.3 mg/L) + ICG-001 (11.2 mg/L) or PTI

(58.5 mg/L) for 6 h. Following incubation, the cells were treated with 2′,7′-dichlorodihydrofluorescein diacetate (DCFH-DA) for 20 min in a 37 °C incubator. Before being observed by CLSM, the cells in light treatment groups were illuminated (638 nm, 0.38 W) for 8 min.

2.7. In vitro cytotoxicity of PTI

To measure the cell viability, 4T1, A549 and 293T cells were respectively seeded into 96-well plates overnight until adherent and then incubated with serious concentrations of ICG-001, PT, PT + ICG-001 or PTI. Subsequently, the light treatment groups were picked up and suffered with illumination (638 nm, 29.8 mW/cm^2) for 12 min. The standard MTT test was applied to measure the cell viability relative to untreated cells.

Live/dead staining was performed to evaluate the cytotoxicity after different treatments. 4T1 cells were incubated with ICG-001 (11.2 mg/L), PT (47.3 mg/L), PT (47.3 mg/L) + ICG-001 (11.2 mg/L) or PTI (58.5 mg/L) for 6 h and suffered with or without 12-min light treatment (638 nm, 29.8 mW/cm^2). After that, the cells were stained with calcein-AM and PI in a 37 °C incubator for 15 min and then observed by CLSM.

Annexin V-FITC/PI assay was taken as another cytotoxicity detection method as well. 4T1 cells were incubated with ICG-001 (4.48 mg/L), PT (18.9 mg/L), PT (18.9 mg/L) + ICG-001 (4.48 mg/L) or PTI (23.4 mg/L) for 6 h in the dark and suffered with or without the irradiation (638 nm, 29.8 mW/cm^2) for 15 min, which were then stained with Annexin V-FITC and PI for 15 min. The cellular fluorescence was detected by flow cytometry.

2.8. Anti-migration test of PTI

The scratch assays were used to evaluate the anti-migration ability of PTI. 4T1 cells were incubated with ICG-001 (11.2 mg/L), PT (47.3 mg/L), PT (47.3 mg/L) + ICG-001 (11.2 mg/L) or PTI (58.5 mg/L) for 6 h and suffered with or without 12-min light treatment (638 nm, 29.8 mW/cm^2). The cells laid at the bottom of the dish were separated by a straight scratch and photographed at 0, 12, and 24 h after irradiation.

2.9. Immunogenic cell death (ICD) induced by PTI

To verify PDT-induced ICD, the expression of calreticulin (CRT) and release of high mobility group protein 1 (HMGB1) were determined through immunofluorescence and Western blot in vitro. For CRT analysis, 4T1 cells were seeded into confocal dishes overnight and then incubated with ICG-001 (22.5 mg/L), PT (94.5 mg/L), PT (94.5 mg/L) + ICG-001 (22.5 mg/L) or PTI (117.0 mg/L) for 6 h. Cells in light treatment groups were picked up for 15-min illumination (638 nm, 29.8 mW/cm^2) and then put back into the incubator for 4 h. Afterward, the cells were fixed with 4% paraformaldehyde for 15 min and then permeabilized by 0.1% Triton X-100 in PBS for 5 min. After being blocked with 10% goat serum, the cells were incubated overnight with anti-CRT antibody (1:500) at 4 °C. Next, the cells were washed by PBS and stained with anti-rabbit IgG (1:500) for 1 h and Hoechst 33342 for 15 min respectively. Finally, the cells were observed by CLSM. Intracellular HMGB1 distribution was also monitored by the same immunofluorescence analysis. But the cells were incubated with anti-HMGB1 antibody (1:500) after blocking with 10% goat serum.

The cell surface exposure of CRT and the nucleus level of HMGB1 were also determined by Western blot. 4T1 cells treated

with ICG-001 (22.5 mg/L), PT (94.5 mg/L), PT (94.5 mg/L) + ICG-001 (22.5 mg/L) or PTI (117.0 mg/L) were lysed by 100 μL radio-immunoprecipitation assay (RIPA) buffer with protease inhibitor. After determining the total protein concentration, 20 μg protein was mixed with the loading buffer and boiled for Western blot. The protein bands obtained through polyacrylamide gel electrophoresis (SDS-PAGE) and membrane transfer were blocked with 5% skim milk powder for 1 h. After cleaning with TBST buffer, the bands were incubated with anti-CRT antibody or anti-HMGB1 antibody overnight on a shaker at 4 °C. The next day, after thoroughly cleaning, the bands were soaked in the anti-rabbit IgG (1:2000) or anti-mouse IgG (1:2000) for 1 h. The ECL reagent was used to detect the position and content of target proteins. Quantitative statistics of grayscale values were analyzed by ImageJ (National Institutes of Health, USA) for each group.

2.10. Interruption of β-catenin signal pathway

4T1 cells seeded in 6-wells plates were incubated with ICG-001 (5.49 mg/L), PT (23.1 mg/L), PT (23.1 mg/L) + ICG-001 (5.49 mg/L) or PTI (28.6 mg/L) for 36 h in darkness. And then the cells were collected for Western blot analysis. The GAPDH was selected for internal reference. Besides, 4T1 cells seeded in 6-wells plate were incubated with ICG-001 (21.9 mg/L), PT (92.1 mg/L), PT (92.1 mg/L) + ICG-001 (21.9 mg/L) or PTI (114.1 mg/L) for 48 h in darkness. Then 1 mL RNAex was added to each well and collect RNA. The quantification of RNA was performed by Nanodrop™ spectrophotometer (Thermo Fisher Scientific, Shanghai, China). The PCR primer sequence was as follows: *Ccl4* forward, 5′-CTCAGCCCTGATGCTTCTCAC-3′; *Ccl4* reverse, 5′-AGAGGGGCAGGAAATCTGAAC-3′; *Tubulin* forward, 5′-TAGCAGAGATCACCAATGCC-3′; *Tubulin* reverse, 5′-GGCAGCAAGCCATGTATTTA-3′. The relative expression level of *Ccl4* was determined by the comparative $2^{-\Delta\Delta Ct}$ method for evaluation.

2.11. Biodistribution of PTI in vivo

Prior to studying the biodistribution of PTI and PT *in vivo*, a primary solid tumor model was constructed on female BALB/c mice by subcutaneous inoculation with 4T1 cells (4×10^6 cells). After 4T1 tumor-bearing mice were i.v. injected with PTI (25 mg/kg) or PT (20 mg/kg) for 0.5, 2, 4, 6, 8 and 12 h, animal imaging was performed. And at 12 h, the mice were sacrificed and the major organs (heart, liver, spleen, lung, kidney) and tumor were harvested for tissue imaging. All animal experiments were conducted according to the protocols approved by the Institutional Animal Care (GY2023-106) and Use Committee of Animal Experiment Center of Guangzhou Medical University (Guangzhou, China).

2.12. Anti-tumor study in vivo

To study the therapeutic effect on primary and metastatic tumors, the lung metastasis model of 4T1 tumor was established on BALB/c mice. After being inoculated with 4T1 cells for 5 days, the mice were i.v. injected 4T1 cells (1×10^6 cells) for the foundation of the lung metastatic model. Next, the tumor-bearing mice were divided into 6 groups randomly. The primary tumor size and body weight of mice were measured and recorded every two days. The tumor volumes were measured by calipers and calculated as shown in Eq. (1):

$$\text{Tumor volume (mm}^3) = \text{Major axis (mm)} \times [\text{Minor axis (mm)}]^2 \times 0.5 \qquad (1)$$

On Days 6, 9, 12 and 20, the mice were injected with ICG-001 (5 mg/kg), PT (20 mg/kg) or PTI (25 mg/kg) *via* caudal vein respectively. 8 h after each administration, the mice in light groups were illuminated with a 638 nm laser (0.68 W) for 8 min. On Day 21, the mice were sacrificed. The weight of tumors, spleens and lungs were measured and photographed. The major organs and tumor tissue were collected for hematoxylin−eosin (H&E) staining. The blood samples were collected for blood biochemical analysis. In addition, tumor slices were also sacrificed for immunofluorescence staining of CCL4, CD103, CD8, Ki-67 and TUNEL.

For analysis of immunocytes in tumors, primary 4T1 tumor-bearing mice were allocated into 6 groups for i.v. injection of ICG-001 (5 mg/kg), PT (20 mg/kg), or PTI (25 mg/kg) on Days 6, 8 and 10. Then the mice in light groups were illuminated (638 nm, 0.68 W) at 8 h post-injection. On Day 11, the tumors and spleens were collected for immunocyte analysis. After cutting the tumor tissue, the tissue lysate was used to lyse it at 37 °C for 1 h, and then the residual tissue blocks were removed by using a filter. After centrifugation at 300*g* (Eppendorf, 5810R, Germany), the red blood cell lysate was treated at room temperature for 15 min. The cells separated by centrifugation were washed with PBS, resuspended and stained with fluorescent antibodies (CD45, CD3, CD4, CD8, CD11C, CD103, CD80, CD86). After staining for 45 min, 4T1 cells labeled with different antibodies were centrifuged, cleaned, and later detected using flow cytometry. The spleens followed the same processing step, ultimately labeling immune cell surface markers with fluorescent antibodies (CD45, CD3, CD4, CD8, CD11C, CD103) and detecting them by flow cytometry.

2.13. Statistical analysis

Statistics were assessed using a One-Way ANOVA with the Tukey−Kramer test (multiple group comparison). A *P*-value of <0.05 was considered to be significant. Data are presented as mean ± SD _

3. Results and discussion

3.1. Synthesis and characterizations of PTI

The photosensitizer conjugated TfR targeting peptide (PT) was synthesized by solid-phase synthesis initially, and the molecular weight was determined by electrospray ionization mass spectrometry (ESI-MS, Thermo Fisher Scientific, Q Exactive Focus, Shanghai, China). The observed fragmentation peak from the result was consistent with expectations, which suggested a successful synthesis of PT (Supporting Information Fig. S1). Subsequently, PTI was constructed using the amphipathic PT to encapsulate hydrophobic ICG-001. In order to get a desirable assembly, TEM and dynamic light scattering (DLS) were utilized to measure the morphology and particle size of various formulations obtained at different feed ratios of PT to ICG-001 (Fig. 1A−C). It turned out that PTI harvested at the ratio of 10:4 (*w/w*) displayed the most structured spherical morphology, the minimum average diameter around 168.7 nm, and the most homogenous distribution with polydispersity index (PDI) of 0.166. Moreover, seven consecutive days of particle size testing
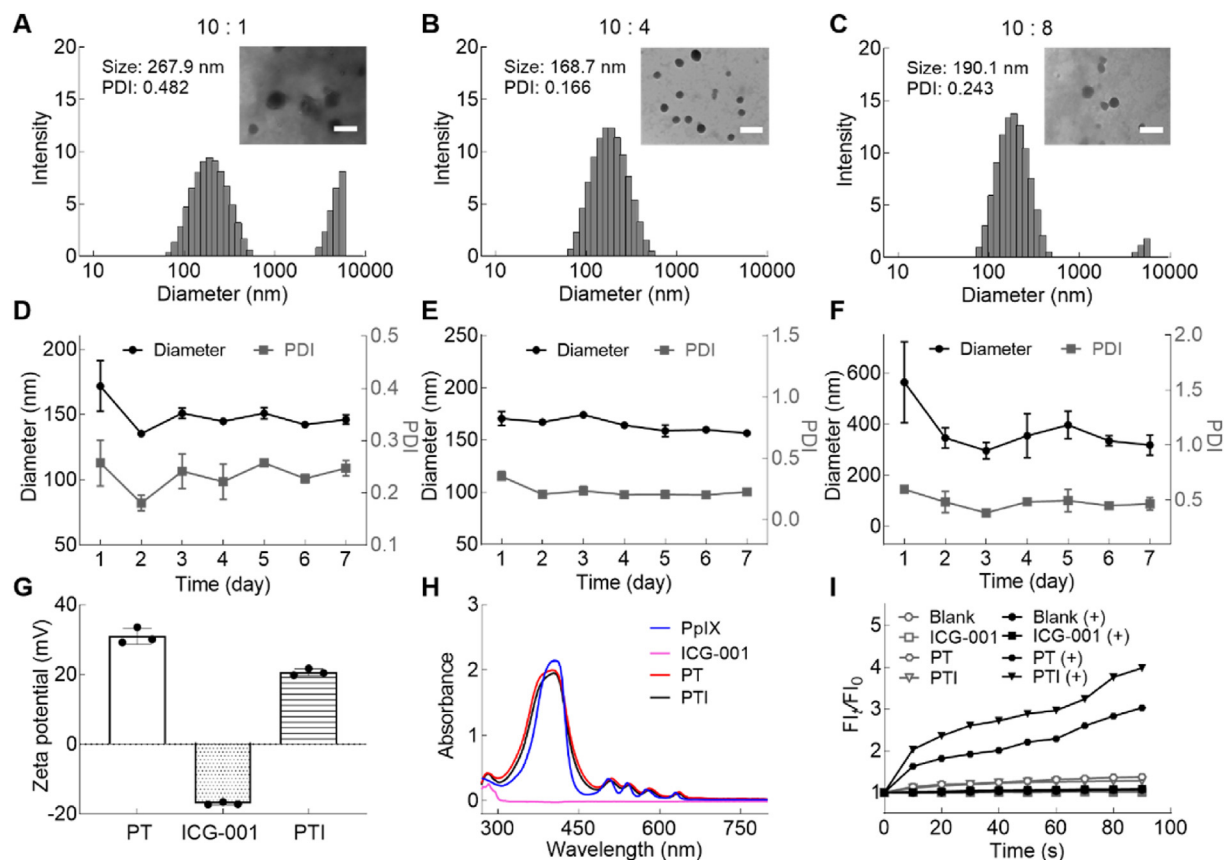
Figure 1 The characterization and optical properties of PTI. Size distributions ($n = 3$) and transmission electron microscope (TEM) images of PTI obtained at the ratios of PT to ICG-001 at (A) 10:1, (B) 10:4 and (C) 10:8. Scale bar: 200 nm; Size and PDI changes of PTI in 7 days under the ratios of (D) 10:1, (E) 10:4 and (F) 10:8; (G) The zeta potential of PT, ICG-001 and PTI. (H) UV−Vis spectra of PpIX, ICG-001, PT and PTI in DMSO. (I) $^1O_2$ generation by ICG-001, PT and PTI with or without illumination. Data are presented as mean $\pm$ SD ($n = 3$).

indicated that the synthesized nanoparticles at this ratio had better water stability in comparison with other groups (Fig. 1D−F). Moreover, the nanoparticles were also kept stable in cell culture medium containing 10% FBS (Supporting Information Fig. S2), implying that the nanomedicine had suitable stability under physiological conditions for biomedical application. Therefore, PT and ICG-001 at the ratio of 10:4 were determined to prepare PTI for further study. The surface zeta potential of PTI was confirmed to be 20.63 ± 0.79 mV (Fig. 1G), which would promote the binding with negative cell membrane for increased cellular uptake. According to the quantitative analysis by HPLC and UV−Vis absorption, PTI was constituted with 19.2% ICG-001 and 80.8% PT (Supporting Information Fig. S3). Besides, ICG-001 was confirmed to be released from PTI under acidic tumor microenvironment (pH 6.5) (Supporting Information Fig. S4). In addition, the UV−Vis spectra of free PpIX, ICG-001, PT and PTI were explored in Fig. 1H. Among which, PTI and PT showed similar characteristic absorbance with PpIX ranging from 300 to 650 nm, suggesting an effective conjugation of PpIX on the peptide. Because of the existence of PpIX, the capability of PTI to generate $^1O_2$ was confirmed using SOSG as a probe. As illustrated in Fig. 1I, PTI upon light could rapidly and consistently enhance the fluorescence of SOSG, demonstrating a lot of $^1O_2$ production. Apparently, the favorable stability and $^1O_2$ production ability of PTI indicated a great potential for photodynamic tumor therapy.

3.2. Cellular uptake

The uptake behavior of nanomedicine by tumor cells would greatly affect the bioavailability and toxicity of drugs. In this work, the uptake efficiencies of PT and PTI were assessed on 4T1 cells applying CLSM and flow cytometry by changing the incubation conditions. As displayed in Fig. 2A, 4T1 cells cultured with PTI and PT were observed a clear trend of cumulative uptake with increasing drug doses. Similar situations could be also seen by expanding the incubation time (Fig. 2B). To further quantify it, flow cytometry was used to analyze the intracellular red fluorescence (Fig. 2C and D). More clearly, both PT and PTI exhibited a concentration and dose-dependent cellular uptake. Excitingly, PTI always had a stronger internalization behavior than PT under the same incubation condition, which illustrated an improved drug delivery efficiency by the nanostructured system.

It is well known that tumor cells have considerably higher levels of TfR expression than normal cells due to their robust proliferative ability[26,27]. Therefore, PTI modified with TfR targeting peptides ought to be more susceptible to infection by tumor cells. To verify it, the uptake ability of different cell lines to PTI was detected by CLSM and flow cytometry (Supporting Information Fig. S5). Compared to normal 293T cells, the tumor cells of 4T1 and A549 had a higher expression of TfR. It was observable that the red fluorescence in 4T1 and A549 cells was significantly stronger than that in 293T cells. The calculations of
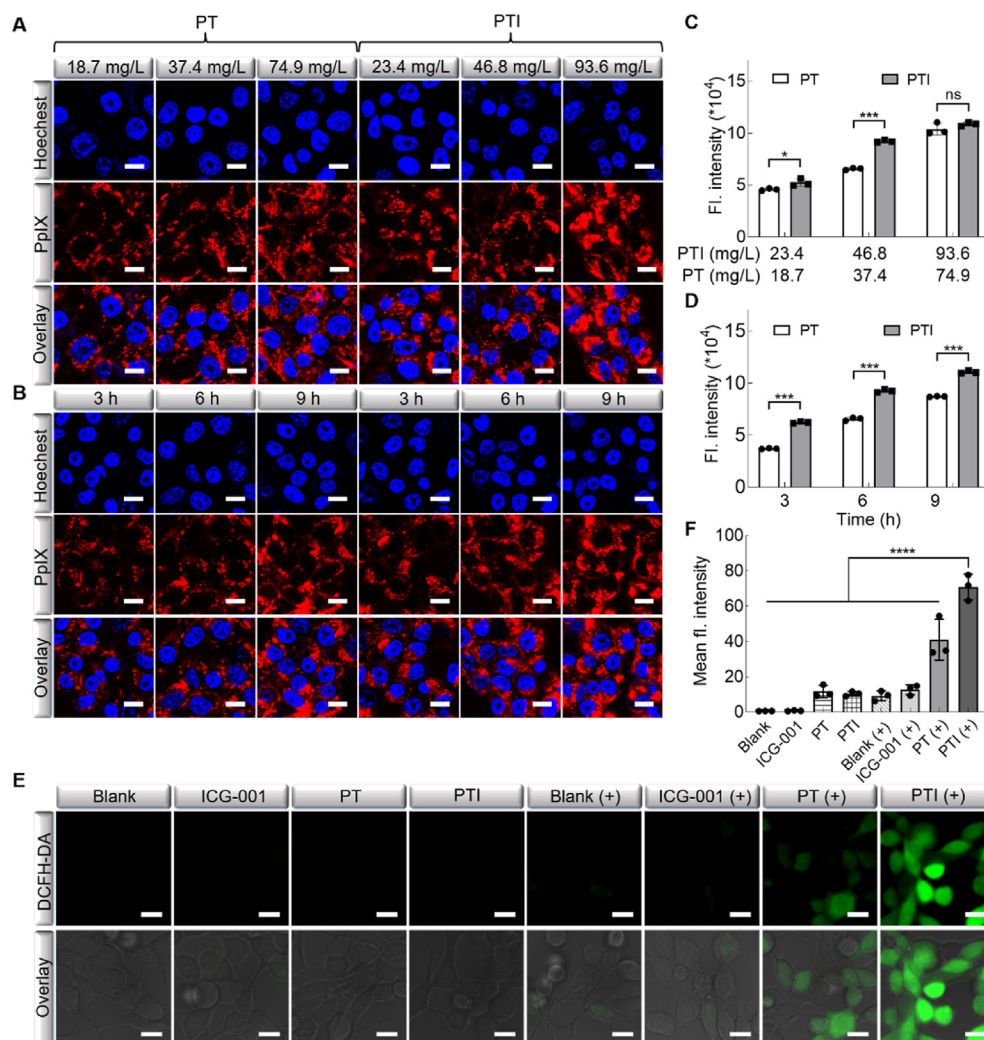
Figure 2 Cell internalization and ROS generation in 4T1 cells. (A) Drug dose and (B) incubation time-dependent uptake behaviors of PT and PTI by 4T1 cells. Flow cytometry analysis of (C) incubation concentration and (D) time-dependent uptake behaviors of 4T1 cells. (E) CLSM images and (F) corresponding fluorescence analysis of 4T1 cells to detect ROS production by DCFH-DA test kit after treated by ICG-001, PT, PTI for 6 h with or without illumination. Scale bar: 10 μm. Data are presented as mean ± SD ($n = 3$). *$P < 0.05$, ***$P < 0.001$, ****$P < 0.0001$ and ns, not significant, was tested *via* a One-Way ANOVA.

flow cytometry further confirmed the propensity of PTI towards tumor cells, in which the fluorescence intensities of 4T1 and A549 cells were 1.47 times and 3.50 times higher than that of 293T cells respectively. This dramatic difference emphasized the absolute superiority of PTI for tumor-targeted drug delivery, which would greatly amplify the therapeutic efficacy of anti-tumor drugs.

3.3. Anti-tumor effect in vitro

The introduction of PpIX endowed PT and PTI with the photodynamic capability of generating ROS under light irradiation. Effective production of ROS was one of the necessary conditions for PDT to achieve anti-tumor efficacy[28]. Accordingly, the fluorescent indicator of DCFH-DA was utilized for intracellular ROS detection. As pictured in Fig. 2E, the non-illuminated group exhibited an invisible green fluorescence. Even under light conditions, there was undetectable fluorescence in the treatment group without photosensitizers. On the contrary, a strong green

fluorescence was observed in the remaining two groups, indicating the ability of PT and PTI to generate ROS at the cellular level upon light conditions. Meanwhile, the results of fluorescence statistics indicated that the PTI treatment group had the highest fluorescence intensity (Fig. 2F), which was appreciably higher than that of the PT treatment group, which agreed well with the CLSM measurement. The better ability of producing ROS by PTI might be owing to the different levels in cellular uptake, which encouraged us to pursue further anti-tumor studies.

First, the cytotoxicity of PTI was evaluated by live/dead cell detection. The results showed that in the light groups of PT, PT + ICG-001 and PT, a substantial increase in dead cells (red fluorescence) and a clear reduction in live cells (green fluorescence) were observed compared to the blank group (Fig. 3A). Statistical analysis of green fluorescence demonstrated that the PTI with light group had the lowest fluorescence intensity (Fig. 3B), indicating that PTI had tremendous aptitude in tumor therapy after light activation. However, compared to the light groups, the red fluorescence of the ICG-001 treatment group was
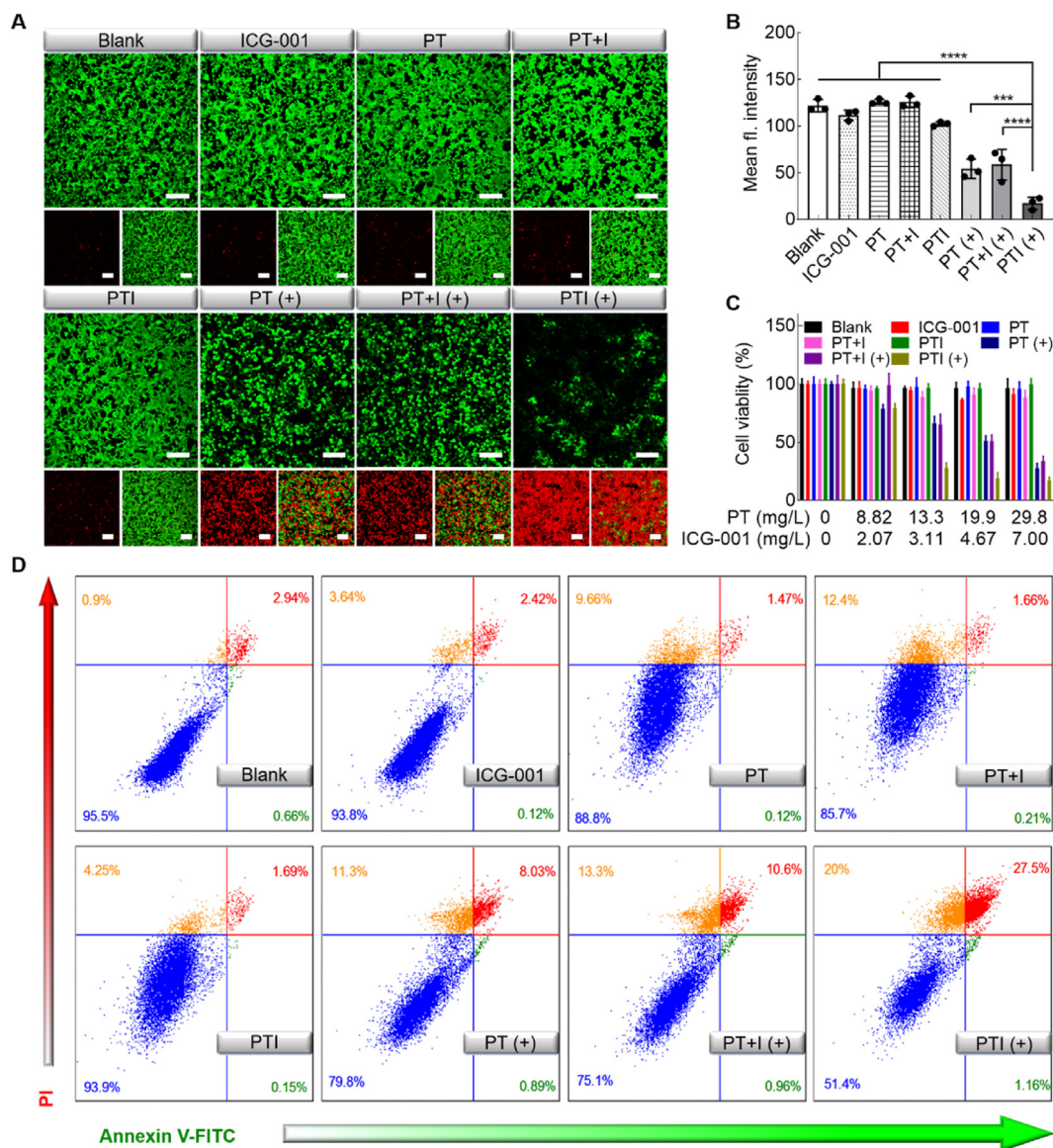
Figure 3 Cytotoxicity of PTI against 4T1 cells. (A) CLSM images of live/dead staining assay and (B) the quantitative green fluorescence analysis of 4T1 cells treated by ICG-001, PT, PT + ICG-001 and PTI with or without illumination (n = 3). Scale bar: 100 μm. (C) MTT assay to detect the viability of 4T1 cells treated by ICG-001, PT, PT + ICG-001 and PTI with or without illumination (n = 4). (D) Flow cytometry measurement to analyze the Annexin V-FITC/PI staining on 4T1 cells treated by ICG-001, PT, PT + ICG-001 and PTI with or without illumination. Data are presented as mean ± SD. ***$P < 0.001$ and ****$P < 0.0001$ was tested *via* a One-Way ANOVA.

extremely weak, implying a limited therapeutic effect. Next, the MTT assay results also displayed that the last three light groups had obvious cytotoxicity, which greatly inhibited the tumor cell proliferation in a dose-dependence manner (Fig. 3C). Among them, PTI with light had an apparently stronger anti-tumor capability, which again highlighted the advantages of nano-structured drug delivery system in tumor treatment. Notably, ICG-001 could hardly retard the cell expansion even increasing the dosage of administration. It was inferred that the *in vitro* anti-tumor effect of PTI was principally triggered by PDT. Moreover, the MTT experiment on A549 cells yielded similar conclusions (Supporting Information Fig. S6A), implying that PTI also had a therapeutic effect on human-derived tumors. However, due to the inefficient uptake of PTI by normal cells, the killing rate of

agents in all light groups did not exceed 30% on 293T cells (Fig. S6B). These results highlighted the superiority of PTI in the treatment of tumors overexpressing TfR.

It was reported that PDT induced cell death mainly through the apoptotic pathway. To further evaluate the PDT efficiency, the apoptotic state of 4T1 cells was measured after similar treatments. As exhibited in Figs. 3D and 4T1 cells were stained with Annexin V-FITC/PI for flow cytometry detection. When without light exposure, over 85% of the cells were alive, and increased apoptotic cells were detected after PDT initiation by light. Nevertheless, less than a quarter of the cells were in apoptosis or necrosis state after PT and PT + ICG-001 treatments upon light. But only about half the cells were not destroyed after the PDT of PTI and the damaged cells were mainly apoptotic or necrotic,

indicating a robust PDT efficiency of PTI to kill tumor cells. The corresponding quantitative data were shown in Supporting Information Fig. S7. Besides, the anti-migration ability of PTI was also evaluated. As shown in Supporting Information Fig. S8, in the dark treatment groups, scratches were gradually occupied by migrating cells over time. However, in the light groups, the PDT could greatly destroy the tumor cells, leading to an alleviative migration effect. Thus, it was supposed that PTI with light could not only inhibit tumor growth, but also weaken the migration ability of tumor cells.

3.4. ICD response induced by PTI

PDT could activate the immune system by inducing ICD and releasing damage-related molecular patterns, such as CRT and HMGB1[29,30]. Immunofluorescence and Western blot analyses were implemented to evaluate the ability of PTI to induce ICD. As proven in Fig. 4A and B, 4T1 cells in PT, PT + ICG-001 and PTI groups with light treatment represented exceedingly bright fluorescence of CRT, while the green fluorescence of HMGB1 displayed the opposite trend. The more HMGB1 was expelled, the correspondingly less HMGB1 was present in the cells. Statistical analysis of immunofluorescence revealed a meaningful disparity in the average fluorescence intensity of cells between the light groups and the dark groups (Fig. 4C and D). It verified that light was an important factor to affect the expression levels of CRT and HMGB1 by triggering PDT, which also highlighted the specificity of phototherapy. The results of Western blot further verified the powerful effect of PDT on engendering ICD that an upsurge in CRT and a decline in HMGB1 were discerned in the PT, PT + ICG-001, and PTI groups with illumination(Fig. 4E). Particularly, in all groups, PTI upon irradiation induced the highest CRT (Fig. 4F) and lowest HMGB1 (Fig. 4G) expressions on 4T1 cells, which was 2.70 and 0.11 times that of the blank group, respectively. However, there were small differences in protein expression levels between the dark treatment groups. These findings demonstrated that PTI-mediated PDT could induce a high expression of CRT on cell membranes and a huge efflux of HMGB1, which could be perceived as two iconic phenomena of ICD.

3.5. Downregulation of PD-L1 and upregulation of CCL4 by β-catenin signal pathway

The expression of PD-L1 could not only prevent tumor cells from being recognized by immune cells, but also inhibit the activation and proliferation of $CD8^+$ T cells, leading to tumor immune escape[31]. WNT/β-catenin signal pathway was considered as one of the signal pathways that upregulated PD-L1 expression[32]. As the pathway inhibitor, the capacity of ICG-001 for reducing PD-L1 expression was estimated by Western blot. As pictured in Supporting Information Fig. S9, 4T1 cells in the PTI group presented a noteworthy downregulation of PD-L1 expression compared to the blank and PT groups. It offered a confirmation that PTI was capable of downregulating the expression of PD-L1 by ICG-001 mediated WNT/β-catenin pathway blocking. Furthermore, statistical analysis of grayscale values of the bands exposed that those groups containing ICG-001, including ICG-001, PT + ICG-001 and PTI groups, could reduce the expression of PD-L1 in 4T1 cells. Among them, the largest downregulation of PD-L1 expression was found in the PTI group, which was 64% of the blank group (Fig. 4H). This significant difference

could be attributed to the increased cell uptake efficiency of PTI, which also implied the potential of PTI in alleviating tumor immune escape.

In tumor cells, the abnormal activation of β-catenin signaling pathway could lead to reduced transcription and insufficient secretion of CCL4, forming an immunosuppressive microenvironment. Therefore, the transcriptional changes of Ccl4 were measured at the cellular level after treatment with PTI by using qPCR. As shown in Supporting Information Fig. S10, the transcription level of Ccl4 was significantly increased in the ICG-001, PT + ICG-001, and PTI groups. Especially in the PTI group, the transcription level of Ccl4 was almost 10 times higher than that of the blank group. These results demonstrated that PTI could efficiently interrupt the binding between β-catenin and CREB to induce the transcription of Ccl4 and downregulation of PD-L1. Besides, the high level of Ccl4 transcription should be positively correlated with the DCs recruitment and activate T cells for immunotherapy.

3.6. Anti-tumor effect in vivo

Above all, the biodistribution of PTI was investigated in vivo. At 0.5, 2, 4, 6, 8, and 12 h after tail vein injection of PTI, the fluorescence on 4T1 tumor-bearing mice was monitored through small animal imaging technology. From the imaging results (Fig. 5A), it could be seen that PTI had a relatively large aggregation at the tumor site at 0.5 h and maintained a decent retention effect in a period of time. After 12 h, the preferable fluorescence accumulation could be still observed on the tumor. Afterward, the mouse was sacrificed and its organs and tumor were taken out for tissue imaging. The aggregation effect of PTI at the tumor tissue could be seen intuitively, further suggesting that PTI had effective tumor targeting (Fig. 5B). As a control, the biodistribution of PT was also assessed (Supporting Information Fig. S11). Although PT also had the TfR targeting property, it exhibited a weaker tumor accumulation than PTI. Thus, it was inferred that the tumor aggregation behavior of PTI should be owing to the TfR targeting peptide and EPR effect. Also, PTI also had an observable concentration on other normal organs, but it might cause low side effects owing to less dark toxicity when without light excitation.

Subsequently, to evaluate the anti-tumor effect of PTI in vivo, a lung metastasis model was established by injecting 4T1 cells into the tail vein of mice loaded with 4T1 primary tumors. Thenceforth, the mice were randomly divided into six groups. After different drug treatments on mice, the size of the transplanted primary tumor was measured every two days to evaluate the anti-tumor effect in vivo. As depicted in Fig. 5C, mice in the PTI with light treatment group performed the maximum diminution in tumor volume. The primary tumor images and weighing results could clearly validate the superior anti-tumor effect of PTI under irradiation as well, while this group of mice had the highest number of cured back tumors (Fig. 5D and E). By contrast, the non-light groups were completely unable to inhibit the primary tumor growth compared to the blank group, demonstrating a very poor therapeutic effect. Similarly, the spleen of the mice was also photographed and weighed (Fig. 5F and G). It could be noted that mice in both PTI and PT groups had a decrease in spleen size and weight under light treatment, resulting from that PDT activated the immune system to alleviate the symptoms of splenomegaly caused by tumors[33,34]. In the H&E staining images of spleen, the PTI with light treatment group showed the clearest edges of the red and white pulp, and the ratio of red to white pulp was the highest
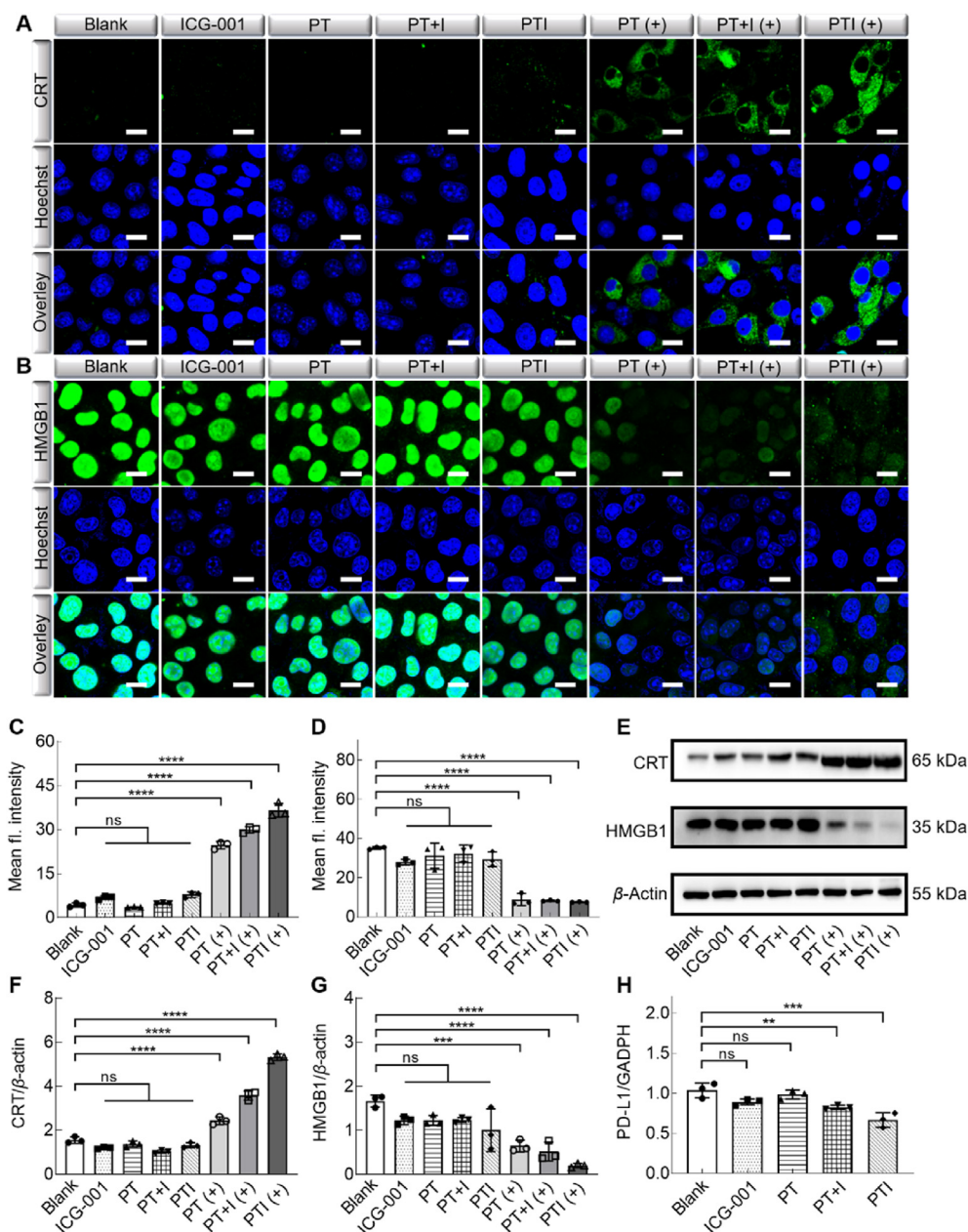
Figure 4 ICD induction and PD-L1 downregulation by PTI. (A) CRT and (B) HMGB1 immunofluorescence staining of 4T1 cells treated by ICG-001, PT, PT + ICG-001 or PTI with or without illumination. Scale bar: 20 μm. Quantitative (C) CRT and (D) HMGB1 immunofluorescence analysis of 4T1 cells after various treatments. (E) Western blot analysis of CRT and HMGB1 expressions on 4T1 cells treated by ICG-001, PT, PT + ICG-001 or PTI with or without illumination. Quantitative analysis of (F) CRT and (G) HMGB1 expressions on 4T1 cells after various treatments. (H) Quantitative analysis of PD-L1 expression on 4T1 cells after treatment with ICG-001, PT, PT + ICG-001 or PTI. Data are presented as mean ± SD (n = 3). **P < 0.01, ***P < 0.001, ****P < 0.0001, and ns, not significant were tested *via* a One-Way ANOVA.

(Fig. 5H), suggesting that PTI could activate the *in vivo* immune system to the greatest extent possible[35]. The images of tumor slices unveiled intensive necrosis in PT and PTI with light groups, with the shrinkage or even disappearance of nucleus in large areas. Additionally, fluorescence staining of TUNEL and Ki-67 also illustrated more cell apoptosis and less cell proliferation in these two groups (Fig. 5I and Supporting Information Fig. S12). The above results all directly confirmed the mighty anti-tumor effect of PDT. In the meantime, upon light irradiation, PTI disclosed a more pronounced ability to damage tumors and inhibit tumor proliferation than PT, which was probably caused by the

immunotherapeutic effect of ICG-001 and the different drug delivery efficiencies.

In order to further explore the immune regulatory role of ICG-001, the immune cells in tumor tissues were analyzed. As a classic β-catenin pathway inhibitor, ICG-001 could remarkably inhibit the immunosuppressive effect of β-catenin caused by abnormal activation in tumors. Studies have discovered that the activation of the β-catenin pathway would lead to unsuccessful recruitment of CD103^{+} DCs by inhibiting the secretion of CCL4[25,36]. Consequently, immunofluorescence staining was resorted to investigate the secretion of tumor CCL4 and the recruitment of DCs after
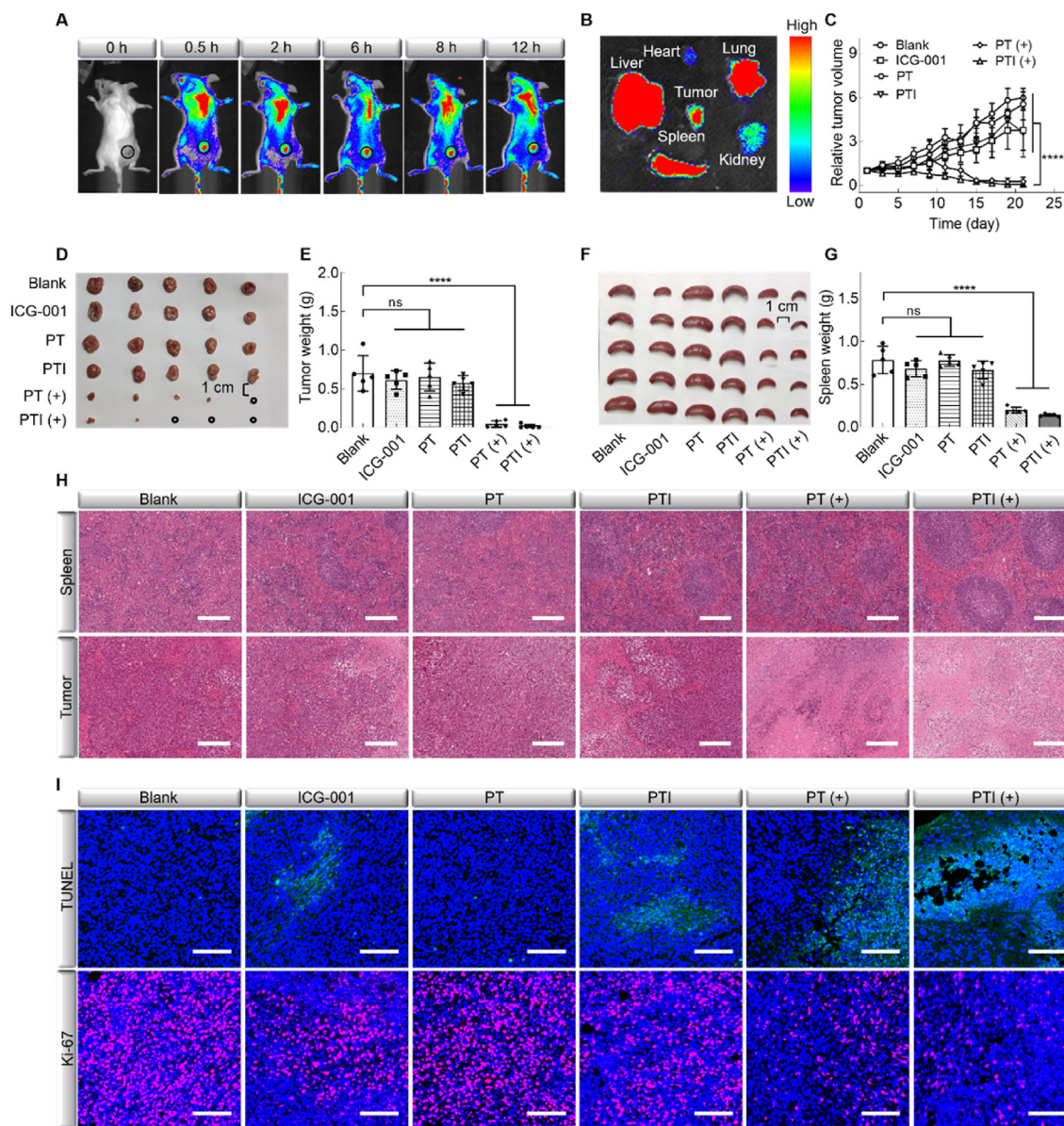
Figure 5 Anti-tumor effect of PTI *in vivo*. (A) Fluorescence images of 4T1 tumor bearing mouse after intravenous injection with PTI for 0 (bright field), 0.5, 2, 4, 8, and 12 h. (B) *Ex vivo* tissue imaging of the mouse after 12 h postinjection. (C) Relative primary tumor growth curves of mice after treatment with ICG-001, PT or PTI in the presence or absence of irradiation in 21 days. (D) Tumor images, (E) the mean tumor weight, (F) spleen images, and (G) spleen weight of mice after various treatments on Day 21. (H) H&E staining images of spleen and tumor tissues after various treatments on Day 21. Scale bar: 200 μm. (I) Immunofluorescence staining of TUNEL (green) and Ki-67 (red) in tumors after various treatments on Day 21. Scale bar: 100 μm. Data are presented as mean ± SD ($n = 5$). ****$P < 0.0001$ and ns, not significant, was tested *via* a One-Way ANOVA.

treatment. The results were consistent with expectations that a large amount of CCL4 secretion was observed in the tumors treated with ICG-001, PT + ICG-001 and PTI (Fig. 6A), while the recruitment of CD103$^+$ DCs also improved noticeably in these three groups (Fig. 6B). Moreover, the fluorescence of CD8 was prominently enhanced compared to the blank group (Fig. 6C), which suggested improved T cells infiltration. The fluorescence statistics also showed similar results (Supporting Information Fig. S13). Of note, PT could also promote the infiltration of CD8$^+$ T cells upon light irradiation, and PTI with light increased more CD8$^+$ T cells than that without light. These results illustrated that the PDT of PT and PTI also played a role in immune

activation by inducing ICD response. Overall, the above results implied that the inhibitory effect of ICG-001 and PTI on the β-catenin pathway could cause an increase in the secretion of CCL4, thereby regulating the distribution of DCs and T cells in tumors. It demonstrated the powerful anti-tumor effect by the combination of phototherapy and immunotherapy.
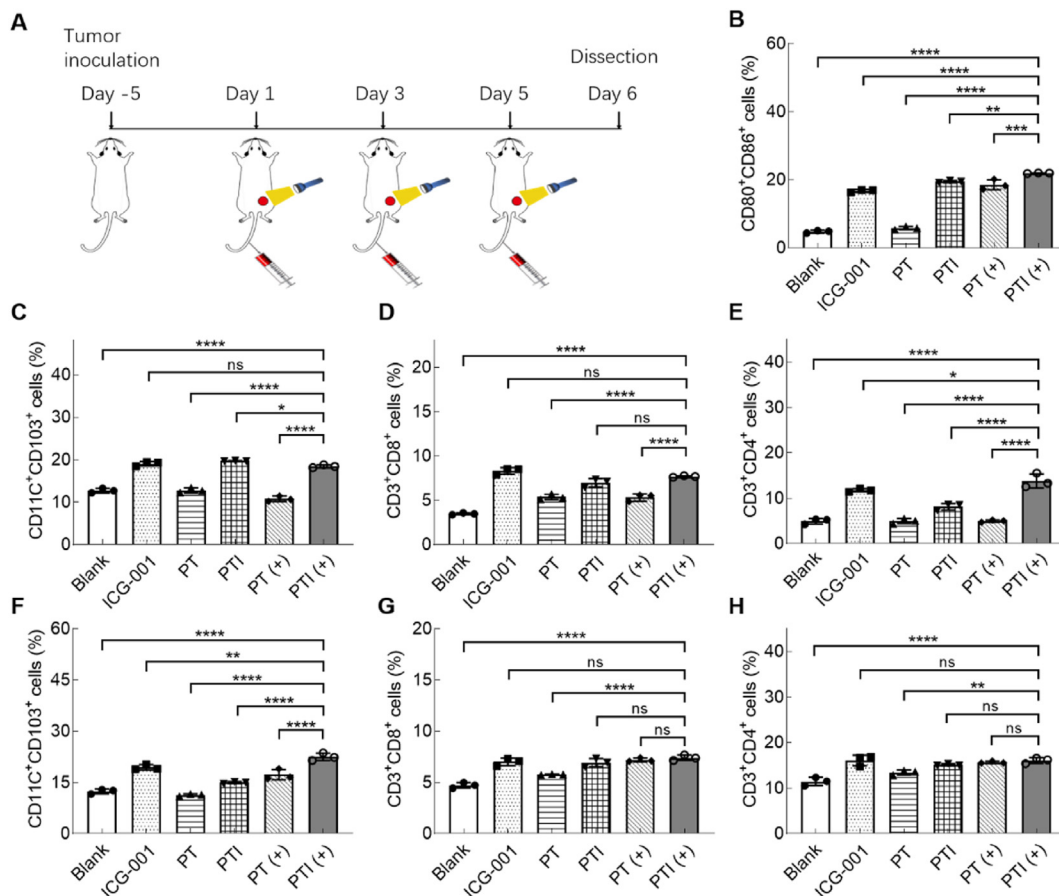
3.7. Immune cells activation in vivo

To investigate the immune effect induced by therapy, the 4T1 tumor-bearing mice were performed for three treatments with ICG-001, PT or PTI, and the tumor was exposed to light at 8 h
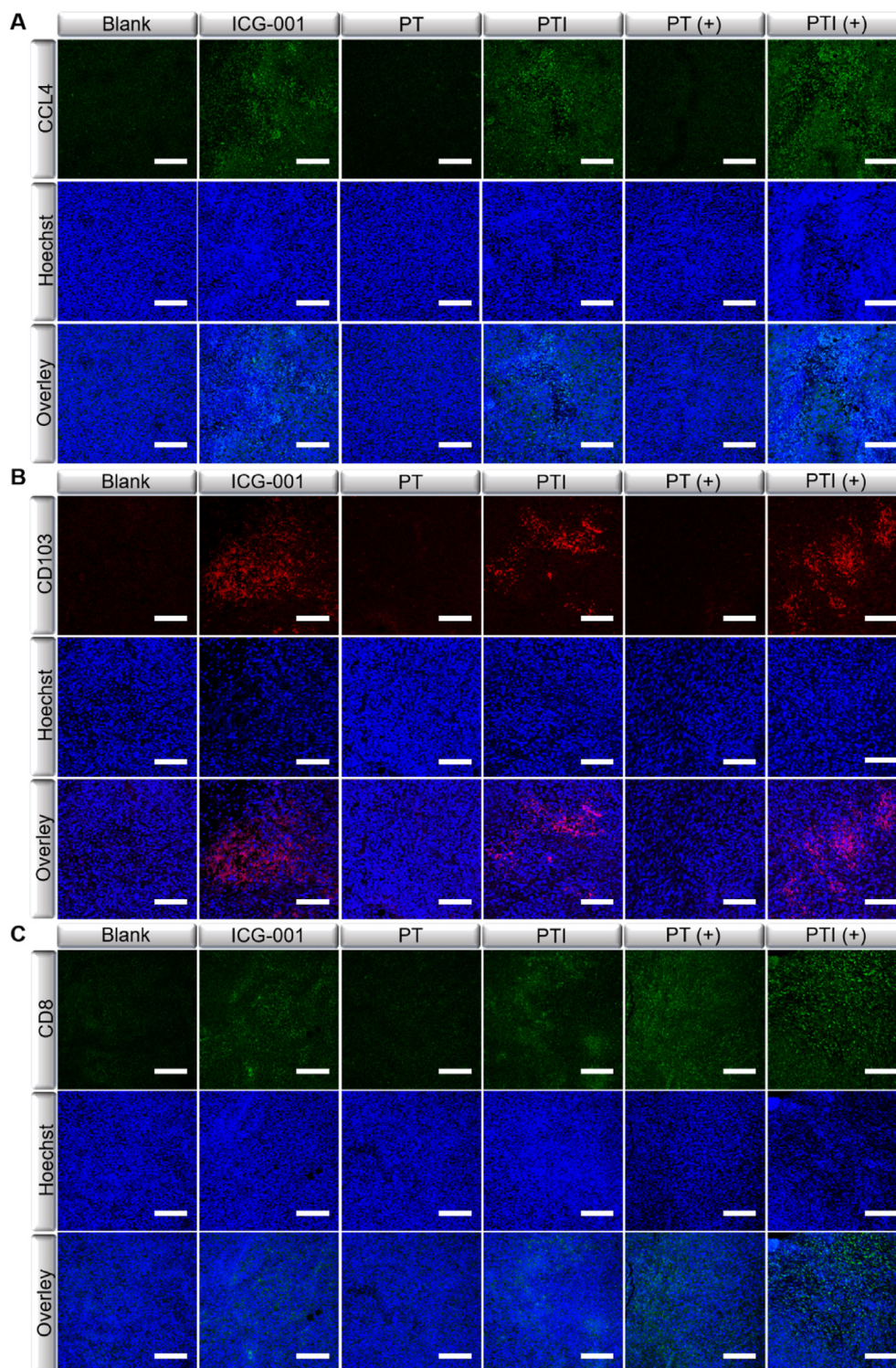
Figure 6 PTI enhanced the infiltration of immune cells in tumor. The immunofluorescence staining of (A) CCL4 (green), (B) CD103 (red) and (C) CD8 (green) in 4T1 tumors after treatment with ICG-001, PT and PTI in the presence or absence of illumination. Scale bar: 100 μm.

post-injection (Fig. 7A). Subsequently, the tumors and spleens of mice were gained for immune cell analysis using flow cytometry (Supporting Information Fig. S14). The results showed that tumors of mice in PTI combined with light group had a maximum upregulation in the proportion of CD80$^+$CD86$^+$ cells compared to other treatment groups (Fig. 7B). Notably, one of the signs of DCs

maturation was the increased expression of surface antigens CD80 and CD86[37]. Thus, the increased proportion of CD80$^+$CD86$^+$ cells meant the promotion of DCs maturation, which should be associated with the ICD cascade induced by the PDT of PTI. Clearly, PTI upon light-induced the strongest ICD response in all groups. To determine whether there was a photothermal effect of

Figure 7 Immune activation *in vivo*. (A) Therapeutic schedule of 4T1 tumor bearing mice for immune cell analysis. Percentages of (B) $CD80^+CD86^+$, (C) $CD11C^+CD103^+$ matured DCs, (D) $CD3^+CD8^+$ and (E) $CD3^+CD4^+$ T lymphocytes in 4T1 tumors treated by ICG-001, PT or PTI with or with light exposure. Percentages of (F) $CD11C^+CD103^+$ matured DCs, (G) $CD3^+CD8^+$ and (H) $CD3^+CD4^+$ T lymphocytes in spleens treated by ICG-001, PT or PTI with or with light exposure. Data are presented as mean $\pm$ SD ($n = 3$). *$P < 0.05$, **$P < 0.01$, ***$P < 0.001$, ****$P < 0.0001$ and ns, not significant, were tested *via* a One-Way ANOVA.

PTI to impact the immune system, the photothermal performance of PTI was evaluated. As shown in Supporting Information Fig. S15, the temperature of PTI was found to rise to 94.2 °F (34.5 °C) after 15 min of laser irradiation. Such a long-term irradiation but a low photothermal effect of PTI indicated a negligible effect to activate the immune system. Thus, it could be concluded that the immunotherapeutic effect of PTI was mainly ascribed to the combination effects of PDT and β-catenin/CREB interruption.

Besides, CD103 could serve as another bona fide DC marker that indicated DC maturation[38,39]. Inhibition of the β-catenin pathway could recruit $CD103^+$ DCs at the tumor site, alleviating the immune suppression microenvironment. As described in Fig. 7C, the proportion of $CD103^+$ DCs in ICG-001, PTI, and PTI with light groups increased a lot compared to other groups, evidencing that the inhibitory effect of ICG-001 on the β-catenin pathway *in vivo* was indeed conducive for the recruitment of $CD103^+$ DCs at the tumor site. After maturation, DCs presented antigens to T cells and initiated T cells infiltrating. Therefore, the increasing trend of $CD3^+CD8^+$ cells was consistent with that of $CD103^+$ DCs (Fig. 7D). Furthermore, PTI with light group exhibited the highest percentage of $CD3^+CD4^+$ T cells (Fig. 7E), which illustrated the best immune activation behavior through β-

catenin pathway blocking. After staining with immune cells isolated from the spleen, flow cytometry detection revealed a sizable upregulation of the proportion of $CD103^+$ DCs in the PTI with light group, which was approximately 1.8 times higher than that in blank and PT groups (Fig. 7F). Meanwhile, the spleens of this group possessed more $CD3^+CD8^+$ and $CD3^+CD4^+$ T cells than that of blank and PT groups (Fig. 7G and H). The above results hinted that the immune activation also exhibited apparent effects in the spleen. Taken together, it could be concluded that PTI was capable of promoting DCs maturation and recruitment, T cells infiltrating and activation to amplify the anti-tumor immune response by ICD induction and β-catenin pathway interruption.

3.8. Anti-metastatic study and biosafety analysis

Immunotherapy is emerging as a promising treatment for metastatic tumor suppression. To assess the anti-metastatic ability of PTI, the lung tissues were obtained from the mice constructing lung metastasis model. It was observed that the mice in PTI with light group had the least number of metastatic nodules on the lung and the H&E staining results also showed the minimum lung metastasis (Fig. 8A). Moreover, there was no obvious metastatic tumor on the organs of heart, liver and kidney in all groups.
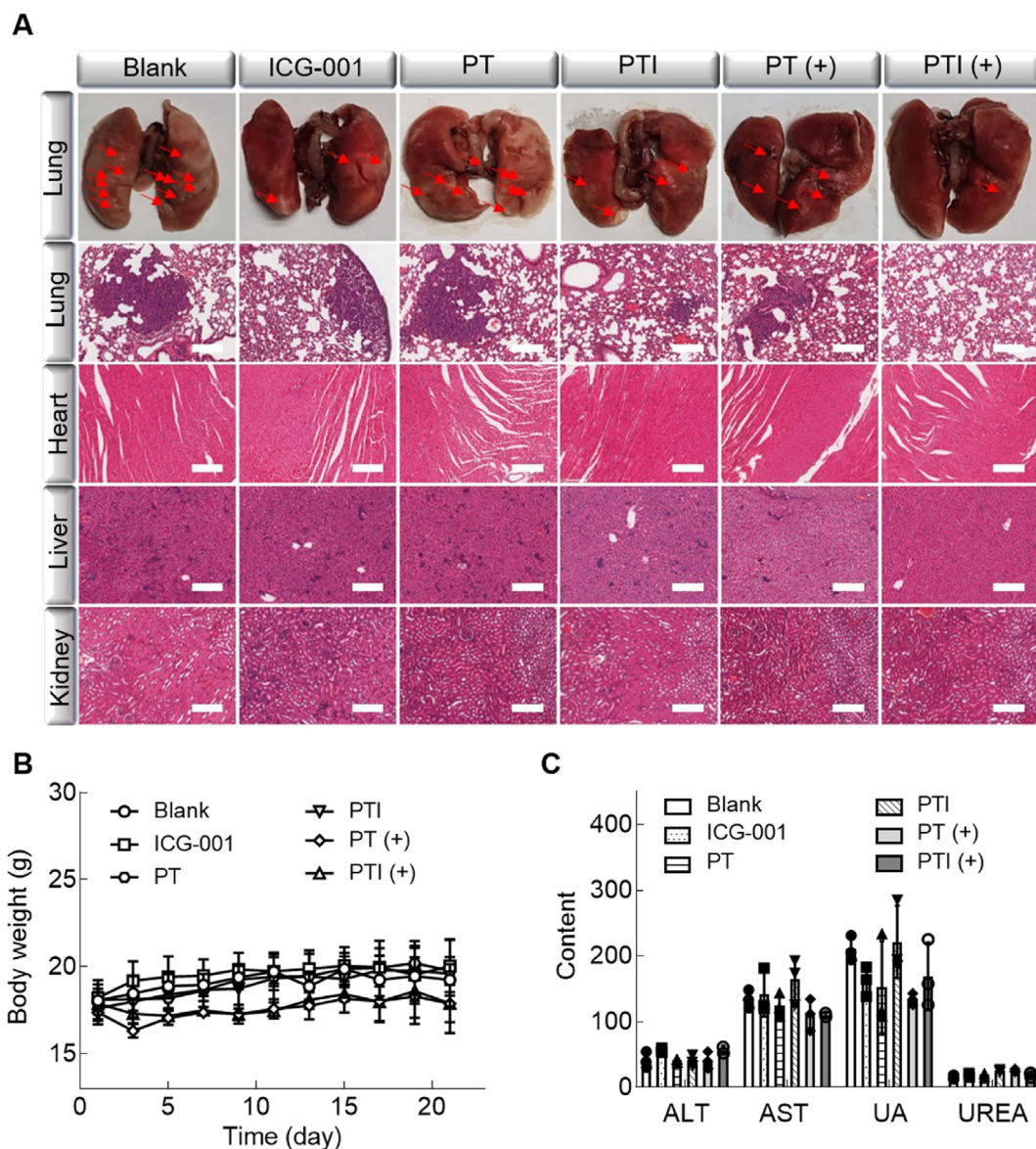
Figure 8 Anti-metastatic study and safety assessment of PTI. (A) Images of lung tissues and H&E staining of lung, heart, liver and kidney of the mice after treatment with ICG-001, PT or PTI in the presence or absence of illumination. Scale bar: 200 μm. (B) The body weight variations of the mice after treatment with ICG-001, PT or PTI in the presence or absence of illumination in 21 days ($n = 5$). (C) Blood biochemical analysis of ALT, AST, UA and UREA after various treatments ($n = 3$).

Meanwhile, these organs remained intact basic functional structures, suggesting that the therapeutic agents caused a low toxicity regardless of their unavoidable aggregation on normal tissues. Notably, although both PT and PTI had a robust tumor eradication effect on primary tumors, the latter had a superior immune activation for inhibition of metastatic tumors. Moreover, PTI could moderately regulate CCL4 secretion and T cells activation by ICG-001-mediated interruption of β-catenin and CREB. To further evaluate the biosafety of drugs, the body weight of mice was monitored during the 21-day treatment. As depicted as Fig. 8B, there were no distinct changes in the weight of the mice from different groups, illustrating reasonable toxicity and safe dose of these therapeutic agents. What's more, the blood biochemistry analysis was also performed, in which the serum levels of ALT, AST, UA, and UREA were all within the normal ranges (Fig. 8C).

It signified that the treatments did not have a significant impact on the liver and kidney functions of mice. The above results indicated that PTI had good biocompatibility and biosafety.

4. Conclusions

In summary, a TfR-targeted immunestimulant (PTI) was designed for photodynamic immunotherapy against metastatic tumors by β-catenin/CREB interruption. The optimized PTI possessed good stability, uniformity and photodynamic property, which could be internalized by tumor cells in a concentration and time-dependent manner. Importantly, PTI was preferable to accumulate at the tumor tissues and cells with TfR overexpression, thereby inducing a robust PDT efficacy to destroy tumors and triggering a strong ICD response to cause CRT exposure and HMGB1 release.

Furthermore, PTI could also interrupt the binding between β-catenin and CREB to regulate the gene transcription, leading to the downregulation of PD-L1 and upregulation of CCL4. The downregulated PD-L1 would promote the immune recognition and clearance of tumor cells to activate anti-tumor immunity. And the upregulated CCL4 contributed to recruiting the DCs to present tumor-specific antigens and facilitate T cell activation and infiltration. Consequently, the improved immunosuppressive microenvironment and enhanced immune activation greatly inhibited the lung metastasis of tumors. This work served as an antibody-free strategy for activating immunotherapy to achieve metastatic tumor treatment, which might facilitate the development of drug combinations and synergistic mechanism for clinical translation.

Acknowledgements

Author contributions

Mengyi Yan: Conceptualization, Investigation, Methodology, Writing − original draft. Xiayun Chen: Investigation, Methodology. Xiaotong Li: Supervision, Investigation. Qianqian Liu: Investigation. Baixue Yu: Investigation. Yi Cen: Investigation. Wei Zhang: Investigation. Yibin Liu: Investigation. Xinxuan Li: Investigation. Ying Chen: Investigation. Tao Wang: Funding acquisition, Supervision. Shiying Li: Conceptualization, Funding acquisition, Project administration, Supervision, Writing − review & editing.

Conflicts of interest

The authors have no conflicts of interest to declare.

Appendix A.   Supporting information

Supporting information to this article can be found online at https://doi.org/10.1016/j.apsb.2024.05.030.

References

1. Reinfeld BI, Rathmell WK, Kim TK, Rathmell JC. The therapeutic implications of immunosuppressive tumor aerobic glycolysis. *Cell Mol Immunol* 2022;**19**:46−58.

2. Gao AQ, Liu X, Lin WL, Wang JN, Wang SY, Si FS, et al. Tumor-derived ILT4 induces T cell senescence and suppresses tumor immunity. *J Immunother Cancer* 2021;**9**:e001536.

3. Fan YB, Li Y, Yao XD, Jin JK, Scott A, Liu B, et al. Epithelial SOX9 drives progression and metastases of gastric adenocarcinoma by promoting immunosuppressive tumour microenvironment. *Gut* 2023;**72**: 624−37.

4. Kerdidani D, Chouvardas P, Arjo AR, Giopanou I, Ntaliarda G, Guo YA, et al. WNT1 silences chemokine genes in dendritic cells and induces adaptive immune resistance in lung adenocarcinoma. *Nat Commun* 2019;**10**:1405.

5. Cerezo-Wallis D, Contreras-Alcalde M, Troulé K, Catena X, Mucientes C, Calvo TG, et al. Midkine rewires the melanoma microenvironment toward a tolerogenic and immune-resistant state. *Nat Med* 2020;**26**:1865−77.

6. Dezhakam E, Khalilzadeh B, Mahdipour M, Isildak I, Yousefi H, Ahmadi M, et al. Electrochemical biosensors in exosome analysis; a short journey to the present and future trends in early-stage evaluation of cancers. *Biosens Bioelectron* 2023;**222**:114980.

7. Wei SC, Duffy CR, Allison JP. Fundamental mechanisms of immune checkpoint blockade therapy. *Cancer Discov* 2018;**8**:1069−86.

8. Marin-Acevedo JA, Kimbrough EO, Lou YY. Next generation of immune checkpoint inhibitors and beyond. *J Hematol Oncol* 2021;**14**: 45.

9. Li KT, Yuan Z, Lyu J, Ahn E, Davis SJ, Ahmed R, et al. PD-1 suppresses TCR−CD8 cooperativity during T-cell antigen recognition. *Nat Commun* 2021;**12**:2746.

10. Poggio M, Hu TY, Pai CC, Chu B, Belair CD, Chang A, et al. Suppression of exosomal PD-L1 induces systemic anti-tumor immunity and memory. *Cell* 2019;**177**. 414−27.e13.

11. Qin G, Wang X, Ye SB, Li YZ, Chen M, Wang SS, et al. NPM1 upregulates the transcription of PD-L1 and suppresses T cell activity in triple-negative breast cancer. *Nat Commun* 2020;**11**:1669.

12. Fan ZW, Wu CY, Chen MM, Jiang YY, Wu YY, Mao RF, et al. The generation of PD-L1 and PD-L2 in cancer cells: from nuclear chromatin reorganization to extracellular presentation. *Acta Pharm Sin B* 2022;**12**:1041−53.

13. Yamaguchi H, Hsu JM, Yang WH, Hung MC. Mechanisms regulating PD-L1 expression in cancers and associated opportunities for novel small-molecule therapeutics. *Nat Rev Clin Oncol* 2022;**19**:287−305.

14. Liu XX, Xie PL, Hao N, Zhang M, Liu Y, Liu PJ, et al. HIF-1-regulated expression of calreticulin promotes breast tumorigenesis and progression through WNT/β-catenin pathway activation. *Proc Natl Acad Sci U S A* 2021;**118**:e2109144118.

15. Yang F, Xu J, Li H, Tan MJ, Xiong XF, Sun Y. FBXW2 suppresses migration and invasion of lung cancer cells *via* promoting β-catenin ubiquitylation and degradation. *Nat Commun* 2019;**10**:1382.

16. Pan JC, Fang S, Tian HC, Zhou CW, Zhao XD, Tian H, et al. lncRNA JPX/miR-33a-5p/Twist1 axis regulates tumorigenesis and metastasis of lung cancer by activating WNT/β-catenin signaling. *Mol Cancer* 2020;**19**:9.

17. Zhang W, Ruan XH, Li YS, Zhi JT, Hu LF, Hou XK, et al. KDM1A promotes thyroid cancer progression and maintains stemness through the WNT/β-catenin signaling pathway. *Theranostics* 2022;**12**: 1500−17.

18. Luke JJ, Bao R, Sweis RF, Spranger S, Gajewski TF. WNT/β-catenin pathway activation correlates with immune exclusion across human cancers. *Clin Cancer Res* 2019;**25**:3074−83.

19. Li R, Hao YH, Roche K, Chen GY, Pan W, Wang AZ, et al. Chemotherapy-induced nanovaccines implement immunogenicity equivalence for improving cancer chemoimmunotherapy. *Biomaterials* 2023;**301**:122290.

20. Sun MY, Liu ZW, Wu L, Yang J, Ren JS, Qu XG. Bioorthogonal-activated *in situ* vaccine mediated by a COF-based catalytic platform for potent cancer immunotherapy. *J Am Chem Soc* 2023;**145**:5330−41.

21. Overchuk M, Weersink RA, Wilson BC, Zheng G. Photodynamic and photothermal therapies: synergy opportunities for nanomedicine. *ACS Nano* 2023;**17**:7979−8003.

22. Zhou ZJ, Zhang L, Zhang ZR, Liu ZM. Advances in photosensitizer-related design for photodynamic therapy. *Asian J Pharm Sci* 2021;**16**: 668−86.

23. Mojarad-Jabali S, Mahdinloo S, Farshbaf M, Sarfraz M, Fatahi Y, Atyabi F, et al. Transferrin receptor-mediated liposomal drug delivery: recent trends in targeted therapy of cancer. *Expert Opin Drug Deliv* 2022;**19**:685−705.

24. Tang L, Zhang R, Wang YS, Zhang XY, Yang YL, Zhao BY, et al. A simple self-assembly nanomicelle based on brain tumor-targeting peptide-mediated siRNA delivery for glioma immunotherapy *via* intranasal administration. *Acta Biomater* 2023;**155**:521−37.

25. Spranger S, Bao R, Gajewski TF. Melanoma-intrinsic β-catenin signalling prevents anti-tumour immunity. *Nature* 2015;**523**:231−5.

26. Jones DT, Trowbridge IS, Harris AL. Effects of transferrin receptor blockade on cancer cell proliferation and hypoxia-inducible factor function and their differential regulation by ascorbate. *Cancer Res* 2006;**66**:2749−56.

27. Singh M, Mugler K, Hailoo DW, Burke S, Nemesure B, Torkko K, et al. Differential expression of transferrin receptor (TfR) in a spectrum of normal to malignant breast tissues: implications for *in situ* and invasive carcinoma. *Appl Immunohistochem Mol Morphol* 2011;**19**:417−23.

28. Sun YX, Zhao DY, Wang G, Wang Y, Cao LL, Sun J, et al. Recent progress of hypoxia-modulated multifunctional nanomedicines to enhance photodynamic therapy: opportunities, challenges, and future development. *Acta Pharm Sin B* 2020;**10**:1382−96.

29. Zhou ZG, Chen JS, Liu Y, Zheng CJ, Luo WJ, Chen LL, et al. Cascade two-stage tumor re-oxygenation and immune re-sensitization mediated by self-assembled albumin-sorafenib nanoparticles for enhanced photodynamic immunotherapy. *Acta Pharm Sin B* 2022;**12**:4204−23.

30. Turubanova VD, Balalaeva IV, Mishchenko TA, Catanzaro E, Alzeibak R, Peskova NN, et al. Immunogenic cell death induced by a new photodynamic therapy based on photosens and photodithazine. *J Immunother Cancer* 2019;**7**:350.

31. Du LY, Lee JH, Jiang HF, Wang CD, Wang SL, Zheng ZH, et al. β-Catenin induces transcriptional expression of PD-L1 to promote glioblastoma immune evasion. *J Exp Med* 2020;**217**:e20191115.

32. Boussiotis VA. Molecular and biochemical aspects of the PD-1 checkpoint pathway. *N Engl J Med* 2016;**375**:1767−78.

33. Castro F, Pinto ML, Pereira CL, Serre K, Barbosa MA, Vermaelen K, et al. Chitosan/γ-PGA nanoparticles-based immunotherapy as adjuvant to radiotherapy in breast cancer. *Biomaterials* 2020;**257**:120218.

34. Steenbrugge J, Breyne K, Demeyere K, De Wever O, Sanders NN, Van Den Broeck W, et al. Anti-inflammatory signaling by mammary tumor cells mediates prometastatic macrophage polarization in an innovative intraductal mouse model for triple-negative breast cancer. *J Exp Clin Cancer Res* 2018;**37**:191.

35. Schwenck J, Schörg B, Fiz F, Sonanini D, Forschner A, Eigentler T, et al. Cancer immunotherapy is accompanied by distinct metabolic patterns in primary and secondary lymphoid organs observed by noninvasive *in vivo* ^{18}F-FDG-PET. *Theranostics* 2020;**10**:925−37.

36. Abdulrahman Z, Santegoets SJ, Sturm G, Charoentong P, Ijsselsteijn ME, Somarakis A, et al. Tumor-specific T cells support chemokine-driven spatial organization of intratumoral immune microaggregates needed for long survival. *J Immunother Cancer* 2022;**10**:e004346.

37. Waisman A, Lukas D, Clausen BE, Yogev N. Dendritic cells as gatekeepers of tolerance. *Semin Immunopathol* 2017;**39**:153−63.

38. Watchmaker PB, Lahl K, Lee M, Baumjohann D, Morton J, Kim SJ, et al. Comparative transcriptional and functional profiling defines conserved programs of intestinal DC differentiation in humans and mice. *Nat Immunol* 2014;**15**:98−108.

39. Broz ML, Binnewies M, Boldajipour B, Nelson AE, Pollack JL, Erle DJ, et al. Dissecting the tumor myeloid compartment reveals rare activating antigen-presenting cells critical for T cell immunity. *Cancer Cell* 2014;**26**:638−52.